

## Structural and magnetic properties of 3d transition metal oxide chains on the (001) surfaces of Ir and Pt

Martin Schmitt,<sup>1</sup> Chong H. Park,<sup>1,2</sup> Paula Weber,<sup>1</sup> Andreas Jäger,<sup>1</sup> Jeannette Kemmer,<sup>1</sup> Matthias Vogt,<sup>1</sup> and Matthias Bode<sup>1,3,\*</sup>

<sup>1</sup>Physikalisches Institut, Experimentelle Physik II, Universität Würzburg, Am Hubland, 97074 Würzburg, Germany

<sup>2</sup>University of British Columbia, 2329 West Mall, Vancouver, British Columbia, Canada

<sup>3</sup>Wilhelm Conrad Röntgen Center for Complex Material Systems (RCCM), Universität Würzburg, Am Hubland, 97074 Würzburg, Germany



(Received 14 June 2019; revised manuscript received 5 August 2019; published 22 August 2019)

We present a survey of the structural and magnetic properties of submonolayer transition metal dioxides on the (001) surfaces of the heavy face-centered cubic noble metals Ir and Pt performed by spin-averaged scanning tunneling microscopy (STM) and spin-polarized (SP) STM. Our STM results confirm that deposition of Co, Fe, Mn, and Cr on the  $(2 \times 1)$  oxygen-reconstructed Ir(001) surface leads to the formation of quasi-one-dimensional chains with a  $(3 \times 1)$  unit cell. As recently predicted by density functional theory [P. Ferstl *et al.*, *Phys. Rev. Lett.* **117**, 046101 (2016)], our SP-STM images of FeO<sub>2</sub> and MnO<sub>2</sub> on Ir(001) show a twofold periodicity along the chains which is characteristic for an antiferromagnetic coupling along the chains. In addition, these two materials also exhibit spontaneous, permanent, and long-range magnetic coupling across the chains. Whereas we find a ferromagnetic interchain coupling for FeO<sub>2</sub>/Ir(001), the magnetic coupling of MnO<sub>2</sub> on Ir(001) appears to be a noncollinear 120° spin spiral, resulting in a  $(9 \times 2)$  magnetic unit cell. On Pt(001), patches of  $(3 \times 1)$ -reconstructed oxide chains could only be prepared by transition metal (Co, Fe, and Mn) deposition onto the cold substrate and subsequent annealing in an oxygen atmosphere. Again SP-STM on MnO<sub>2</sub>/Pt(001) reveals a very large,  $(15 \times 2)$  magnetic unit cell which can tentatively be explained by a commensurate 72° spin spiral. Large-scale SP-STM images reveal a long-wavelength spin rotation along the MnO<sub>2</sub> chain.

DOI: [10.1103/PhysRevB.100.054431](https://doi.org/10.1103/PhysRevB.100.054431)

### I. INTRODUCTION

Significant progress has been achieved toward a thorough understanding of magnetically ordered states in solid-state materials [1]. Over the past 40 years spin structures with increasing complexity were detected. Whereas collinear ferro- or antiferromagnetism governed by the competition of exchange, magnetocrystalline anisotropy, and dipolar interactions initially dominated the scientific debate, we have witnessed a focusing on more complex noncollinear magnetic states since the advent of the current century [2]. This development was—at least partially—made possible by the development of advanced surface analysis and microscopy tools which allow for the detection of magnetic signals with unprecedented sensitivity and spatial resolution. In the context of this contribution spin-polarized scanning tunneling microscopy (SP-STM) will be of particular interest. This technique utilizes the tunnel magnetoresistance effect between a magnetic surface and a spin-polarized tip to obtain information about the sample's spin structure with atomic resolution [3]. SP-STM allowed for the first direct imaging of antiferromagnetic surfaces [4] and domain walls [5], as well as of frustrated Néel spin states with antiphase domains [6]. Furthermore, it turned out that the spin-orbit-induced Dzyaloshinskii-Moriya interaction (DMI), which was

previously considered in some rare cases only, can be very significant at surfaces and interfaces. For example, it turned out that the Mn monolayer on W(110), which has initially been assumed to be a simple collinear and uniaxial antiferromagnet [7,8], instead forms a chiral spin cycloid [9].

Recently a group of novel quasi-one-dimensional 3d transition metal oxides (TMOs) was discovered which can conveniently be prepared by self-organized growth on the (001) surfaces of the heavy face-centered cubic (fcc) metals Ir and Pt [10,11]. For Ni, Co, Fe, and Mn on Ir(001) and also for Co on Pt(001) a structural  $(3 \times 1)$  unit cell was observed by low-energy electron diffraction (LEED). In either case scanning tunneling microscopy (STM) reveals a surface morphology which is characterized by long and highly periodic chains oriented along the  $[110]$  and  $[\bar{1}\bar{1}0]$  high-symmetry directions of the (001) surface. The structure of the TMO chains on fcc(001) surfaces as proposed by Ferstl *et al.* [10] is schematically represented in Fig. 1. Within each chain we find two oxygen atoms (red) between nearest-neighbor transition metal atoms (yellow). The TMO chains sit above empty substrate rows, held in place by the oxygen atoms.

Indeed, density functional theory (DFT) calculations reproduced the experimentally determined structural properties well [10]. These theoretical investigations also predicted highly interesting intrachain magnetic couplings, ranging from nonmagnetic (NM) NiO<sub>2</sub> via ferromagnetic (FM) coupling for CoO<sub>2</sub> and FeO<sub>2</sub> to an antiferromagnetic (AFM) interaction along MnO<sub>2</sub> chains on Ir(001) [10]. Furthermore,

\*Corresponding author: bode@physik.uni-wuerzburg.de

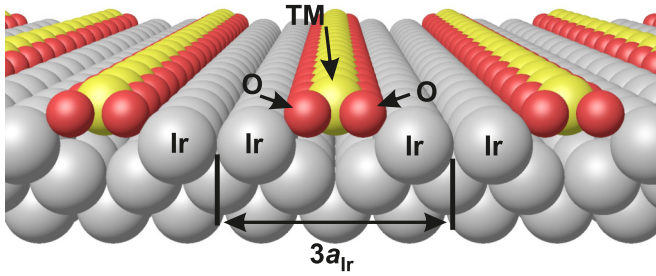


FIG. 1. Structure model of transition metal oxide chains on Ir(001) as proposed in Ref. [10]. The transition metal atom chains sit above empty substrate rows, held in place by the oxygen atoms. The interchain spacing corresponds to  $3a_{\text{Ir}}$ .

an AFM coupling was predicted for  $\text{CoO}_2$  chains on Pt(001) [11]. In general, the coupling strength was found to be much stronger along the chains (up to 44 meV per TM atom) than across adjacent chains (a few meV). It should be kept in mind, however, that the calculations performed in Refs. [10] and [11], which are qualitatively summarized in Table I, were restricted to collinear spin configurations. Noncollinear magnetic structures, such as the Néel state, spin spirals, skyrmions, or helical spin structures, which can potentially arise from frustration [6], higher-order exchange [12,13], or the DMI [9], have not been considered. To verify the predictions of Ferstl *et al.* [10,11] we recently studied the magnetic structure of  $\text{MnO}_2$  chains on Ir(001) by means of spin-polarized scanning tunneling microscopy (SP-STM) [14]. In addition to the AFM coupling along the chains predicted by Ferstl *et al.* [10] an indirect  $120^\circ$  magnetic coupling across the chains was observed. This surprising finding was rationalized in terms of a Dzyaloshinskii-Moriya-enhanced Ruderman-Kittel-Kasuya-Yosida (RKKY) interaction [14]. These earlier results obtained on  $\text{MnO}_2/\text{Ir}(001)$  showed that this indirect magnetic coupling mechanism which was previously only observed for assemblies of single atoms or clusters on Pt(111) surfaces [15,16] can also result in chiral magnetic order in laterally extended structures.

The purpose of this paper is to investigate the magnetic structure of a broad range of  $(3 \times 1)$ -ordered TMO chains on (001) surfaces of the heavy fcc noble metals Ir and Pt by SP-STM. The paper is organized as follows: The SP-STM technique and the experimental procedures applied for substrate cleaning, oxidation, and transition metal deposition

TABLE I. Magnetic moments and magnetic coupling of one-dimensional TMOs along (intrachain) and across (interchain) adjacent chains and corresponding energy gain as predicted by DFT in Refs. [10] and [11].

	Ir(001)				Pt(001)
	$\text{NiO}_2$	$\text{CoO}_2$	$\text{FeO}_2$	$\text{MnO}_2$	$\text{CoO}_2$
$\mu$ ( $\mu_{\text{B}}$ )	0.00	1.96	3.55	3.62	
Intrachain coupling ( $\parallel$ )	NM	FM	AFM	AFM	AFM
$\Delta E_{\parallel}$ (meV)		25	44	27	
Interchain coupling ( $\perp$ )		FM	AFM	AFM	
$\Delta E_{\perp}$ (meV)		4	9	0.4	

are briefly described in Sec. II. Results for the two substrates, i.e., Ir(001) and Pt(001), will be presented separately in Sec. III A and Sec. III B, respectively. SP-STM measurements were performed on the oxides of Co, Fe, Mn, and Cr on Ir(001) and for Co and Mn on Pt(001). Whereas no magnetic contrast could be detected for Co and Cr, the magnetic intrachain coupling observed for the other transition metals is in agreement with DFT predictions [10,11]. In addition, our results also reveal magnetic ordering across the chains. Whereas we find a collinear coupling across the chains for  $\text{FeO}_2$  on Ir(001), the indirect interchain coupling of  $\text{MnO}_2$  on both Ir(001) and Pt(001) is found to be helical, resulting in complex spin structures with surprisingly large magnetic unit cells.

## II. EXPERIMENTAL PROCEDURES

STM experiments were performed in a two-chamber ultrahigh vacuum (UHV) system with a base pressure  $p \leq 5 \times 10^{-11}$  mbar. Clean Ir(001) and Pt(001) surfaces were prepared by annealing cycles in an oxygen atmosphere followed by cycles of sputtering and annealing without oxygen. After this procedure the well-known  $(5 \times 1)$  reconstruction of Ir(001) as well as the  $(26 \times 118)$  structural unit cell of Pt(001) was confirmed [17–20].

Closely following the procedures described by Ferstl and co-workers [10], the clean Ir(001) surface was then exposed to molecular oxygen resulting in a  $(2 \times 1)$ -reconstructed surface. The oxygen pressure indicated by our quadrupole mass spectrometer was  $p_{\text{O}_2} = 1 \times 10^{-8}$  mbar, but the local pressure is assumed to be about two orders of magnitude higher since the gas nozzle is located just a few centimeters above the sample surface. On this oxygen-reconstructed Ir surface we deposited one third of a monolayer (ML) of either Co, Fe, Mn, or Cr. All 3d transition metals were vaporized with commercial e-beam evaporation sources (EFM3). Whereas Co and Fe were evaporated from wires with a diameter of 2 mm, Mn and Cr lumps were loaded into Mo crucibles. Upon 3d transition metal deposition the sample was again annealed in an oxygen atmosphere, resulting in the  $(3 \times 1)$  structure of TMO chains [10]. Since the annealing temperature  $T_{\text{ann}}$  required for optimal TMO chain quality was found to depend on the transition metal element, the specific values will be given below. Due to the higher stability of the Pt(001) reconstruction to oxygen exposure the preparation of TMO chains on Pt(001) is slightly different [11,21]. Namely, the 3d transition metal was directly evaporated onto the reconstructed surface and only subsequently annealed in an oxygen atmosphere [11]. To verify the structural properties of the TMO chains the samples were transferred into a home-built low-temperature scanning tunneling microscope (LT-STM) where they were scanned with an electrochemically etched polycrystalline W tip at an operation temperature of  $T \approx 5.5$  K. All images were obtained in the constant-current mode with bias voltage ( $U$ ) applied to the sample. When using spin-polarized tips in SP-STM measurements the recorded tunneling current  $I$  can be written as

$$I = I_0 + P_t P_s \cos \theta, \quad (1)$$

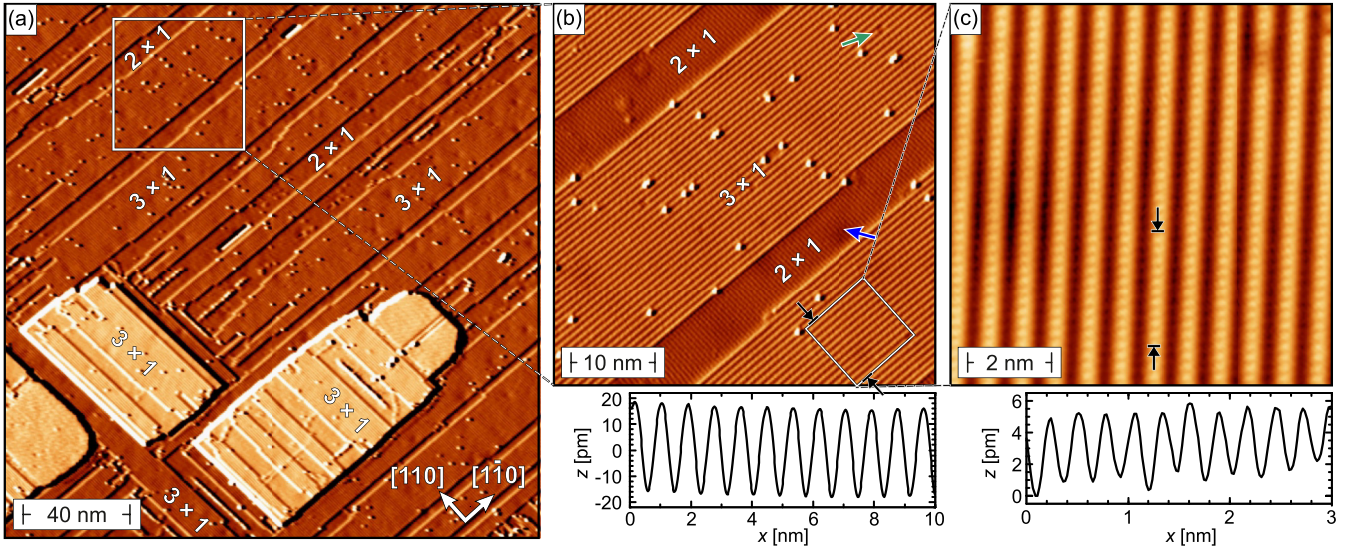


FIG. 2. (a) Overview scan of a sample with coexisting  $(3 \times 1)$ -ordered  $\text{CoO}_2$  chains and  $(2 \times 1)$  oxygen-reconstructed areas on  $\text{Ir}(001)$ . (b) Higher-magnification image of the area marked by a white square in (a) revealing an orthogonal orientation row orientation of  $(2 \times 1)$ - and  $(3 \times 1)$ -ordered areas. The line profile in the bottom panel confirms a  $3a_{\text{Ir}}$  periodicity perpendicular to the  $\text{CoO}_2$  chains. (c) Atomic-resolution scan of the area marked by a box in (b). The line profile verifies the  $\times 1$  periodicity along the  $\text{CoO}_2$  chains. Scan parameters: (a), (b)  $U = 1$  V,  $I = 300$  pA; (c)  $U = 50$  mV,  $I = 1$  nA. All scans performed with a nonmagnetic W tip.

where  $I_0$  is the spin-averaged contribution to the tunneling current. The second term in Eq. (1) represents the magnetization-direction-dependent variation of the total current which depends on the angle  $\theta$  between tip  $P_t$  and sample  $P_s$  polarization. For SP-STM the W tips were flashed by electron bombardment and coated with either Fe or Cr. To unambiguously determine the in-plane or out-of-plane sensitivity of the magnetic SP-STM tips they were characterized on a reference system. In the present case we used the Fe double layer (DL) on  $\text{W}(110)$  which exhibits a well-known inhomogeneous spin spiral, thereby offering the possibility to identify the in-plane and out-of-plane components of the tip magnetization in a single measurement [22–24].

As we will discuss below, we could not obtain magnetic contrast on some TMOs even though earlier DFT calculations predict them to order magnetically. This raises the question of the detection limit of SP-STM. In fact, the surface spin structures of numerous elements have successfully been imaged in the past, including rare-earth metals, such as Gd [25] and Dy [26], or the antiferromagnetic  $3d$  metal Cr [27]. The Gd magnetic moment is largely carried by the  $4f$  shell ( $7 \mu_B$ ) which is energetically located well below the Fermi level and therefore cannot contribute to the tunneling current. For  $\text{Gd}(0001)$  it has been shown that the SP-STM contrast originates from a  $d_{z^2}$ -like surface state which carries a relatively low magnetic moment  $\mu \approx 0.35 \mu_B$  only [28]. In the case of Cr, measurements were performed at room temperature, i.e., at a relatively high reduced temperature  $T/T_N \approx 0.94$  (Néel temperature  $T_N = 311$  K). At this temperature the magnetic moment only amounts to about 40% of its ground-state value. Nevertheless, for both  $\text{Gd}(0001)$  and for  $\text{Cr}(001)$  the surface magnetic structure could clearly be imaged. Considering these earlier results we assume that the detection limit of SP-STM is well below a surface moment of  $1 \mu_B$ .

### III. RESULTS

#### A. TMO chains on $\text{Ir}(001)$

##### 1. $\text{CoO}_2/\text{Ir}(001)$

After evaporation of Co onto the oxidized  $\text{Ir}(001)$  surface at room temperature the sample was annealed at  $T_{\text{ann}} \approx 870$  K at an oxygen partial pressure  $p_{\text{O}_2} = 1 \times 10^{-8}$  mbar. During the TMO chain growth process every third Ir surface atom is expelled from the surface layer. It was previously observed for  $\text{MnO}_2$  on  $\text{Ir}(001)$  [10,14] that—at sufficiently high annealing temperature—these atoms form extended islands or even recombine at step edges with existing surface terraces. A similar behavior can be observed in Fig. 2(a), where monatomic rectangular-shaped islands occur with step edges along the  $[110]$  and  $[1\bar{1}0]$  high-symmetry directions of the substrate.

Closer inspection of the terraces in Fig. 2(b) shows the coexistence of the  $(2 \times 1)$  oxygen reconstruction and the  $(3 \times 1)$  TMO structure along the high-symmetry directions. Furthermore, Fig. 2(b) reveals that the stripes of the  $(2 \times 1)$  reconstruction are generally oriented perpendicular to the  $(3 \times 1)$ -ordered  $\text{CoO}_2$  chains, possibly due to the incommensurability of  $(2 \times 1)$  oxygen-reconstructed and  $(3 \times 1)$ -ordered TMO chains. The presence of oxygen-reconstructed areas without Co possibly indicates that the amount of deposited Co was slightly below one third of a ML. With a density of about  $0.03 \text{ nm}^{-2}$  the most frequent defects are pointlike protrusions on the TMO chains. Their height amounts to about 80 pm, consistent with typical values for transition metal adatoms. Therefore, we assume that these protrusions are caused by either excess Co or Ir atoms which were expelled from the surface layer but remained on the  $\text{CoO}_2$  chains. Furthermore, a few depressions in the chains can be recognized (one of which is marked by the green arrow). Since these depressions are centered where one would expect

a maximum in a periodic chain in the absence of a defect, it appears reasonable to preliminarily assign them to Co vacancies. Both types of defects with similar characteristics will also appear for the other transition metals studied. In addition, we occasionally observe weak circular depressions (see blue arrow) which have also been observed on the bare Ir(001) and are assigned to subsurface defects.

To verify the structural properties of the  $\text{CoO}_2$  on Ir(001) we measured a line profile perpendicular to the chains in the bottom right corner of the STM image displayed in Fig. 2(b). It is plotted at the bottom of Fig. 2(b). The periodicity of  $(828 \pm 30)$  pm agrees well with the expected value of  $3a_{\text{Ir}} = 813$  pm [29]. Additionally, the atomic-resolution scan shown in Fig. 2(c) and the corresponding line section shown in the bottom panel also confirm the  $\times 1$  periodicity with an atomic distance of  $(278 \pm 10)$  pm along the TMO chains.

After structural analysis we prepared magnetic Cr/W tips and Fe/W tips for SP-STM measurements. As documented in the Supplemental Material, these out-of-plane and in-plane sensitive tips were thoroughly tested by imaging the domain and domain wall structure of the Fe DL on W(110), respectively [30]. Although these tests clearly confirmed the magnetic imaging capabilities of our SP-STM tips before and after the measurements on the  $\text{CoO}_2$  chains on Ir(001), we never observed any magnetic contrast on the  $(3 \times 1)$  structure of  $\text{CoO}_2$  chains (not shown). This result is not necessarily in contradiction with the ferromagnetic order predicted in Ref. [10] because we have to keep in mind that the imaging of magnetic spin structures by SP-STM relies on the existence of domains or other spatial variations of the projection of the local sample magnetization onto the fixed magnetization of the tip. Therefore, the ferromagnetic domains could remain undetected if their size was much larger than the scan size. In this context future spatially averaging techniques, such as the magneto-optical Kerr effect, might be useful to clarify this open issue.

## 2. $\text{FeO}_2/\text{Ir}(001)$

The next transition metal element with one electron less in the  $3d$  shell is Fe. It has been predicted that  $\text{FeO}_2$  on Ir(001) exhibits an AFM order along the chains [10]. Just like for the preparation of  $\text{CoO}_2$  chains described in Sec. III A 1, Fe was evaporated at room temperature on the  $(2 \times 1)$ -reconstructed O/Ir(001) surface and immediately annealed at  $T_{\text{ann}} \approx 970$  K in an oxygen atmosphere ( $p_{\text{O}_2} = 1 \times 10^{-7}$  mbar). The overview scan in Fig. 3(a) shows two flat terraces separated by a monatomic substrate step edge. The absence of rectangular islands indicates that all Ir atoms expelled from the substrate had the chance to diffuse to step edges. Close inspection reveals that the chains are oriented along the  $[110]$  direction on the upper (left) terrace whereas they are oriented in the  $[\bar{1}\bar{1}0]$  direction on the lower (right) terrace. The density of the pointlike defects on top of the chains amounts to about  $0.06 \text{ nm}^{-2}$ . Similarly to what was discussed in the preceding Sec. III A 1, we believe that the most likely origin of these protrusions is a slight overdosing of the surface with Fe such that some atoms cannot be accommodated within the resulting Fe oxide chain structure. We would like to note

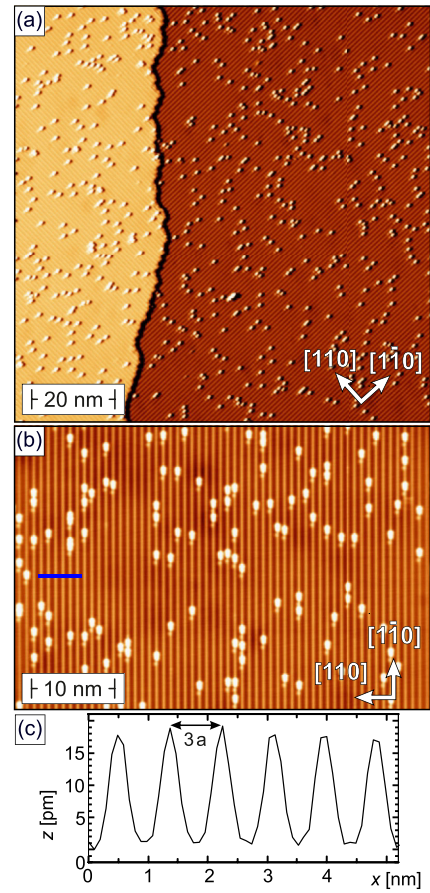


FIG. 3. (a) Overview scan of  $\text{FeO}_2/\text{Ir}(001)$  with chains running in the  $[110]$  direction on the upper and  $[\bar{1}\bar{1}0]$  direction on the lower terrace. (b) Higher-resolution scan on the lower terrace. (c) Line profile along the blue line in (b). The periodicity of the stripes amounts to  $(855 \pm 50)$  pm. Scan parameters: (a), (b)  $U = -1$  V,  $I = 300$  pA, nonmagnetic W tip.

that the teardrop-shaped appearance of the protrusions is an imaging artifact caused by the unusual shape of the tip used in this experiment.

For structural analysis of the  $\text{FeO}_2$  chains a higher-resolution scan on the lower terrace is shown in Fig. 3(b). The periodicity across the chains along the blue line is determined by the line profile shown in Fig. 3(c). Again we find periodicity of  $(855 \pm 50)$  pm which is in good agreement with the value expected for a  $(3 \times 1)$  reconstruction, i.e.,  $3a_{\text{Ir}} = 813$  pm. To complete the structural analysis an atomic-resolution scan of  $\text{FeO}_2$  is presented in Fig. 4(a). Line sections drawn between the black arrows in Fig. 4(a) which are presented in Fig. 4(c) (black lines) show a periodicity of  $(278 \pm 10)$  pm, consistent with the Ir lattice constant  $a_{\text{Ir}} = 271$  pm. Furthermore, an additional weak stripe in the center of the  $(3 \times 1)$  unit cell in Fig. 4(a) can be recognized in between the chains. A similar observation was reported by Ferstl *et al.* [10] and assigned to an electronic signal of the Ir double rows separating adjacent TMO chains. The magnetic structure of this surface was investigated by SP-STM with an out-of-plane sensitive Cr-coated W tip. The result is presented in Fig. 4(b). Direct comparison with Fig. 4(a) reveals a

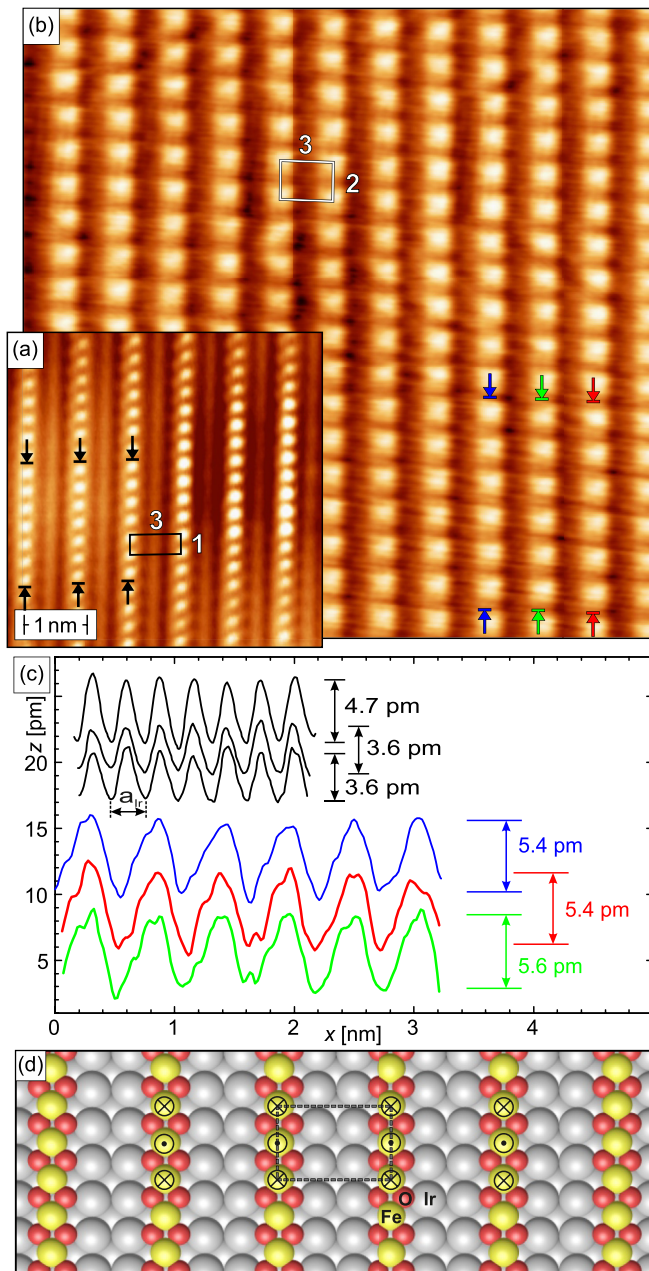


FIG. 4. (a) Atomic-resolution scan of  $\text{FeO}_2$  chains on  $\text{Ir}(001)$  obtained with a nonmagnetic W tip. The atoms along the chains are separated by one Ir lattice constant  $a_{\text{Ir}} = 271$  pm. (b) SP-STM image obtained with an out-of-plane Cr/W tip. Comparison to (a) reveals a period along the chains corresponding to  $2a_{\text{Ir}} = 542$  pm resulting in a  $(3 \times 2)$  magnetic unit cell. (c) Line profiles measured along the chains at the position indicated by the arrows in (a) and (b). (d) Schematic illustration of the  $(3 \times 2)$  collinear magnetic order. While the magnetic coupling is AFM along the chains, the interaction of adjacent chains is FM. Scan parameters: (a)  $U = -10$  mV,  $I = 20$  nA; (b)  $U = 50$  mV,  $I = 5$  nA.

doubled period along the chains. This impression is corroborated by the line profiles presented in Fig. 4(c) which have been taken in between the three pairs of colored arrows and clearly show a period  $2a_{\text{Ir}} = 542$  pm along the chains. The doubling is caused by the magnetoresistance effect which

leads to a tunneling current which scales with the projection of the sample magnetization onto the tip magnetization [cf. Eq. (1)]. The most obvious explanation for the observed doubling of the period along the chain is an AFM coupling. Furthermore, the maxima and minima of adjacent  $\text{FeO}_2$  chains in Figs. 4(b) and 4(c) are aligned, thereby clearly indicating a FM coupling across the chains. The fact that all magnetic line profiles show the same corrugation essentially excludes any noncollinear magnetic order, such as spin spirals or frustrated Néel spin states, but rather supports that  $\text{FeO}_2/\text{Ir}(001)$  exhibits collinear magnetism.

Our experimental results obtained on  $\text{FeO}_2$  chains on  $\text{Ir}(001)$  indicate a  $(3 \times 2)$  magnetic unit cell which is marked as a box in Fig. 4(b) and schematically illustrated in Fig. 4(d). The AFM coupling observed along the chains is in agreement with recent theoretical predictions [10]. Our opinion is that it is quite reasonable to assume that this AFM along the chains is caused by superexchange mediated by the fully occupied oxygen  $2p$  orbitals [31]. Although a much weaker AFM coupling across the chains was predicted in Ref. [10], we experimentally observe spontaneous, permanent, and long-range FM interchain coupling at  $T = 5$  K. At the moment we can only speculate on why theory and experiment deviate. Since adjacent TMO chains are separated by two nonmagnetic Ir rows this order cannot be mediated by direct exchange. As we will point out below for  $\text{MnO}_2$  chains on  $\text{Ir}(001)$ , it appears that the strong spin-orbit interaction of the Ir substrate plays a decisive role for the formation of the magnetic ground state. Potentially, similar effects are also relevant for  $\text{FeO}_2/\text{Ir}(001)$ . More advanced theoretical considerations will be necessary to fully elucidate the coupling mechanism.

### 3. $\text{MnO}_2/\text{Ir}(001)$

Our SP-STM results presented in the preceding section were in good agreement with DFT predictions regarding the intrachain magnetic coupling [10] but also indicate that some aspect of the interchain coupling may not have been captured with sufficient accuracy. Since DFT qualitatively predicts the same intrachain magnetic coupling for  $\text{MnO}_2/\text{Ir}(001)$  as for  $\text{FeO}_2$  it is highly interesting to experimentally investigate also this sample system. The preparation of  $\text{MnO}_2$  chains is very similar to the TMOs discussed so far. Also in this case Mn is deposited onto the oxidized  $\text{Ir}(001)$  surface at room temperature. In our experience the best surface quality can be achieved when choosing a slightly higher annealing temperature  $T_{\text{ann}} \approx 1020$  K. This results in a sample topography with roughly rectangular islands, as exemplarily presented in the overview scan of Fig. 5(a). The  $(3 \times 1)$ -ordered  $\text{MnO}_2$  chain structure covers almost the entire sample surface such that no regions with the oxygen-induced  $(2 \times 1)$  reconstruction of  $\text{Ir}(001)$  remain visible. Typical  $(3 \times 1)$  domains are about 20 to 40 nm wide and often hundreds of nm long. Adjacent domains are separated by either orientational or antiphase domain boundaries. Similarly to the cases for other TMO chains on  $\text{Ir}(001)$  we observe several defects which are located on top of the chains. For example, in Fig. 5(b) 12 single protrusions, one dimer, and a vacancy in a  $\text{MnO}_2$  row can be recognized. This corresponds to a defect density of only  $0.015 \text{ nm}^{-2}$ , well below what has been determined for  $\text{CoO}_2$  and  $\text{FeO}_2$

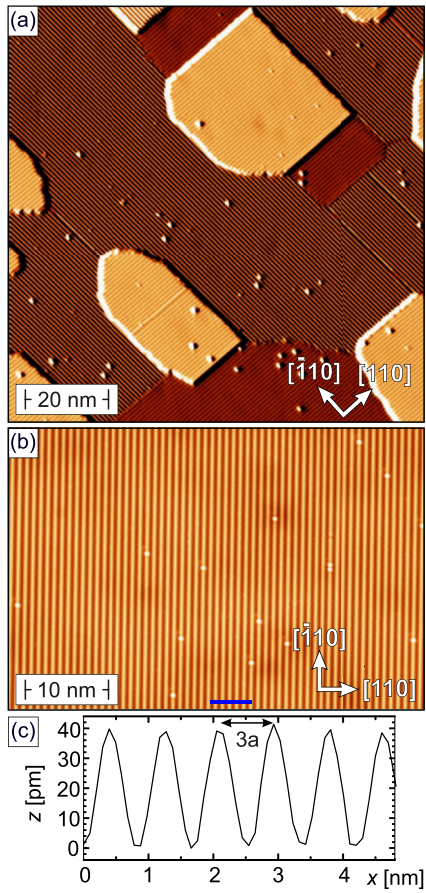


FIG. 5. (a) Overview scan of MnO<sub>2</sub> chains on Ir(001). Domains with stripes of the  $(3 \times 1)$  structure orientated along the  $[\bar{1}10]$  and the  $[110]$  direction can be recognized. (b) Spin-averaged STM image of an atomically flat surface area showing a few defects only. (c) Line profile measured along the blue line in (b) confirming an interchain distance of  $3a_{\text{Ir}}$ . Scan parameters:  $U = 1$  V,  $I = 300$  pA, nonmagnetic W tip.

in Secs. III A 1 and III A 2, respectively. The periodicity of the stripes can be determined by the line profile presented in Fig. 5(c). In agreement with the expected  $(3 \times 1)$  structure it amounts to  $(840 \pm 50)$  pm. As shown in Fig. 6(a) this  $(3 \times 1)$  superstructure has been imaged with atomic resolution in a spin-averaging STM experiments by using a nonmagnetic W tip. The corrugation and periodicity along the chains in Fig. 6(a) can be determined from the line profiles presented in Fig. 6(c) (black lines). These data sets clearly show that any chain exhibits a corrugation of  $z \approx 2.2$  pm only and a periodicity of  $(287 \pm 20)$  pm. In addition, Fig. 6(a) also reveals a small corrugation in between the chains which can possibly be assigned to Ir pairs.

In Fig. 6(b) we present spin-polarized measurements of MnO<sub>2</sub> chains on Ir(001) which were performed with an in-plane sensitive magnetic Cr/W tip. We would like to note that these results, which were obtained in a different experimental run on a newly prepared sample with a different SP-STM tip, qualitatively reproduce earlier results [14]. Quantitative differences, such as a different corrugation, are attributed to the fact that the two tips probably differ in their spin

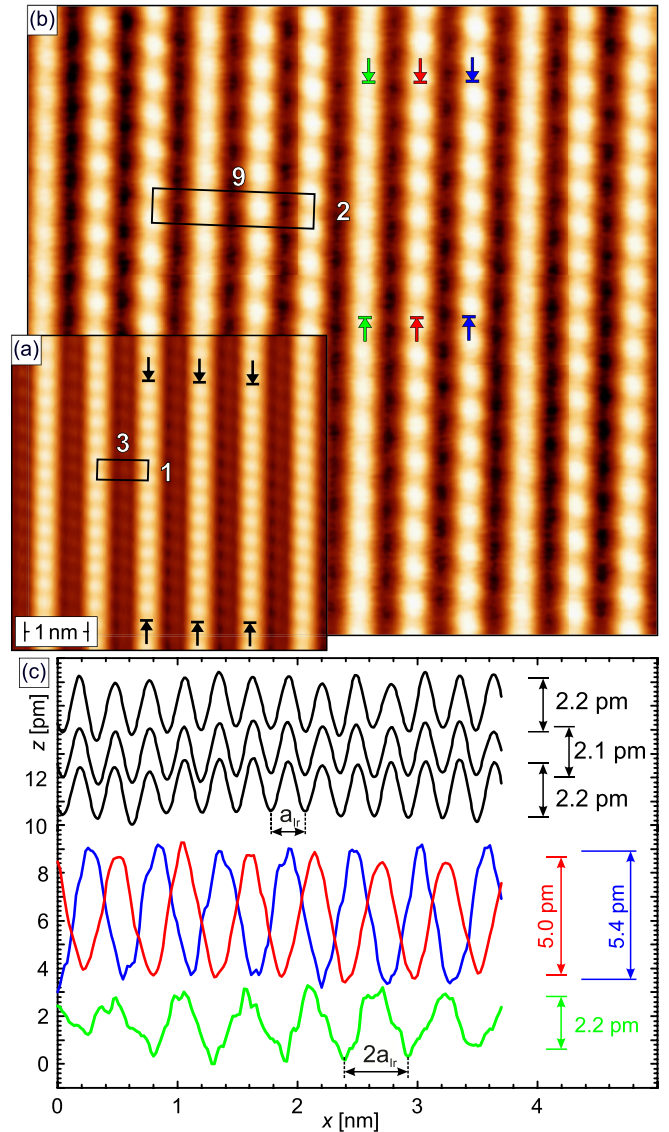


FIG. 6. (a) Atomic-resolution scan of the MnO<sub>2</sub> chains on Ir(001) measured with a nonmagnetic W tip showing the  $(3 \times 1)$  unit cell. (b) SP-STM image of MnO<sub>2</sub>/Ir(001) obtained with an in-plane sensitive Cr-coated W tip. The period along the stripes corresponds to  $2a_{\text{Ir}}$  indicating AFM order along the chain. The magnetic contrast of adjacent chains is modulated by phase and corrugation changes resulting in a  $(9 \times 2)$  magnetic unit cell. (c) Line profile measured along three adjacent chains in (a) without (black) and in (b) with magnetically sensitive tips (colored). Scan parameters: (a)  $U = -300$  mV,  $I = 3$  nA; (b)  $U = 200$  mV,  $I = 300$  pA.

polarization and quantization axes. Similarly to the results on FeO<sub>2</sub> discussed in Sec. III A 2 the use of a magnetic probe tip leads to a doubling of the measured corrugation period which now corresponds to  $2a_{\text{Ir}}$  along the chains. Furthermore, comparison of adjacent chains reveals a periodic variation of the corrugation. This can qualitatively be realized by comparing the chain marked with red arrows in Fig. 6(b) with the chains on the left and right which are marked green and blue, respectively. The green chain on the left obviously exhibits a much weaker corrugation. In contrast, no obvious difference

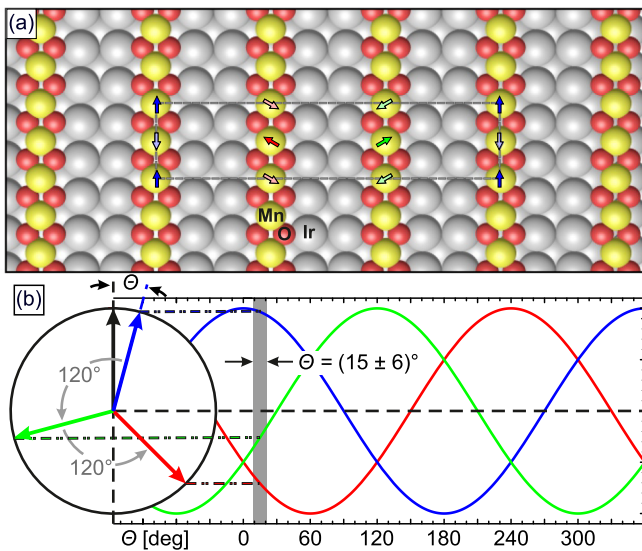


FIG. 7. (a) Schematic illustration of the  $(9 \times 2)$  magnetic unit cell of  $\text{MnO}_2$  chains on  $\text{Ir}(001)$ . The arrows indicate the spin direction of the corresponding Mn atoms. (b) Sketch of the SP-STM signal expected for the proposed chiral  $120^\circ$  spin spiral. The corrugation and the phase shift observed in Fig. 6(b) can be explained by an angle  $\Theta = (15 \pm 6)^\circ$  between tip polarization (black arrow) and the TMO chain with highest corrugation (blue line).

between the contrast strength of the red and blue line can be recognized, but the positions of maxima and minima of the chain marked with blue arrows are interchanged with respect to the red line. The colored line profiles presented in Fig. 6(c) allow for a more quantitative comparison. In agreement with our qualitative assessment the green chain exhibits the smallest corrugation of 2.2 pm whereas both the blue and red lines have a much higher corrugation of about 5 pm. In addition, we can also recognize the phase shift of  $a_{\text{Ir}}$  between the red and blue lines. Detailed comparison shows that the blue chain has a slightly higher corrugation than the red chain. Together with the above-mentioned periodicity  $2a_{\text{Ir}}$  along the chains these SP-STM observations suggest a  $(9 \times 2)$  magnetic unit cell.

The experimental observations on  $\text{MnO}_2$  chains can be explained by a spin structure as schematically illustrated in Fig. 7(a). Each  $\text{MnO}_2$  chain is AFM ordered whereby the easy axis always lies within the surface plane. The azimuthal orientation rotates by  $120^\circ$  between adjacent  $\text{MnO}_2$  chains such that the magnetic structure repeats every third chain. These two ingredients, i.e., the AFM order along and the tripled magnetic period perpendicular to the  $\text{MnO}_2$  chains, result in a  $(9 \times 2)$  magnetic unit cell as indicated in Fig. 6(b). As sketched in Fig. 7(b), this magnetic structure can explain the corrugation and the phase relation observed by SP-STM in Figs. 6(b) and 6(c). In this representation the black arrow represents the tip magnetization and the colored arrows represent the quantization axes of the respective chains.

Proceeding from right to left in the  $(9 \times 2)$  magnetic unit cell in Fig. 7(a) we can recognize that the magnetic structure is governed by an in-plane counterclockwise spin spiral with a rotation angle of  $120^\circ$  between adjacent chains. Since the

blue arrow exhibits the largest projection onto the black arrow it will—according to Eq. (1)—give the strongest magnetic contrast in SP-STM measurements, symbolized by the dot-dashed line in Fig. 7(a). As a result of the spin spiral the green and red arrows are aligned antiparallel with respect to the tip. In the case of an AFM intrachain coupling this will unavoidably lead to a phase shift between the blue spin chain as compared to the green and red spin chain. Based on this representation we can nicely reproduce the corrugations extracted from Fig. 6(c) by an angle between the blue chain and the tip polarization of  $\theta = (15 \pm 6)^\circ$ , indicated by a gray region in Fig. 7(b).

In a recently published paper the observation of a chiral  $120^\circ$  spin spiral which is mediated across two atomic rows of the nonmagnetic  $\text{Ir}(001)$  substrate was explained by a Dzyaloshinskii-Moriya type (DM) enhancement of the RKKY interaction [14]. This interaction, which was already predicted in 1980 [32], leads to a magnetic coupling which is at the same time indirect and chiral. Evidence for DM-enhanced indirect magnetic coupling had previously been observed on some surface-deposited clusters [15,16,33,34] and Dy/Y superlattices [35]. Indeed, state-of-the-art density functional theory calculations could successfully reproduce not only the antiferromagnetic coupling along the chains but also explain the period of the chiral magnetic structure across the chains [14]. However, the experimental data suggest a spin spiral which predominantly rotates within the surface plane, corresponding to a Dzyaloshinskii-Moriya vector  $\mathbf{D}$  oriented along the surface normal. This surprising result cannot be explained within the structural model deduced from quantitative low-energy electron diffraction data [10], which would result in a  $\mathbf{D}$  vector within the surface. The discrepancy might be caused by yet unconsidered effects of structural domain boundaries or relaxation effects. Additional DFT calculations and field-dependent SP-STM measurements will be necessary to fully resolve this open question.

#### 4. $\text{CrO}_2/\text{Ir}(001)$

Motivated by the observation of an unexpected non-collinear magnetism in  $(3 \times 1)$ -ordered  $\text{MnO}_2$  chains on  $\text{Ir}(001)$  we tried to extend the series of self-organized TMO chains to Cr which is the left neighbor of Mn in the periodic table of elements. Since the growth of  $\text{CrO}_2$  chains was not part of the study by Ferstl *et al.* [10] it will be discussed here in detail. The preparation follows the principle of the known TMO chains and comprises the evaporation of Cr onto the  $(2 \times 1)$   $\text{O}/\text{Ir}(001)$  surface at room temperature. Subsequently, the sample was annealed in an oxygen atmosphere ( $p_{\text{O}_2} = 1 \times 10^{-8}$  mbar) at a temperature  $T_{\text{ann}} \approx 1070$  K.

The resulting sample topography and its structural analysis are shown in Fig. 8. Already in the overview scan presented in Fig. 8(a) we can recognize stripes orientated along the  $[\bar{1}10]$  direction. We count 145 pointlike defects with a typical height of several 10 up to 100 pm on top of the stripes, corresponding to a defect density below 0.015 per  $\text{nm}^2$ . Moreover, some protrusions are visible that we already identified on clean  $(5 \times 1)$  reconstructed  $\text{Ir}(001)$  surfaces. The periodic arrangement of the stripes with an interstripe distance of  $(846 \pm 40)$  pm is shown at higher resolution in Fig. 8(b). This value is

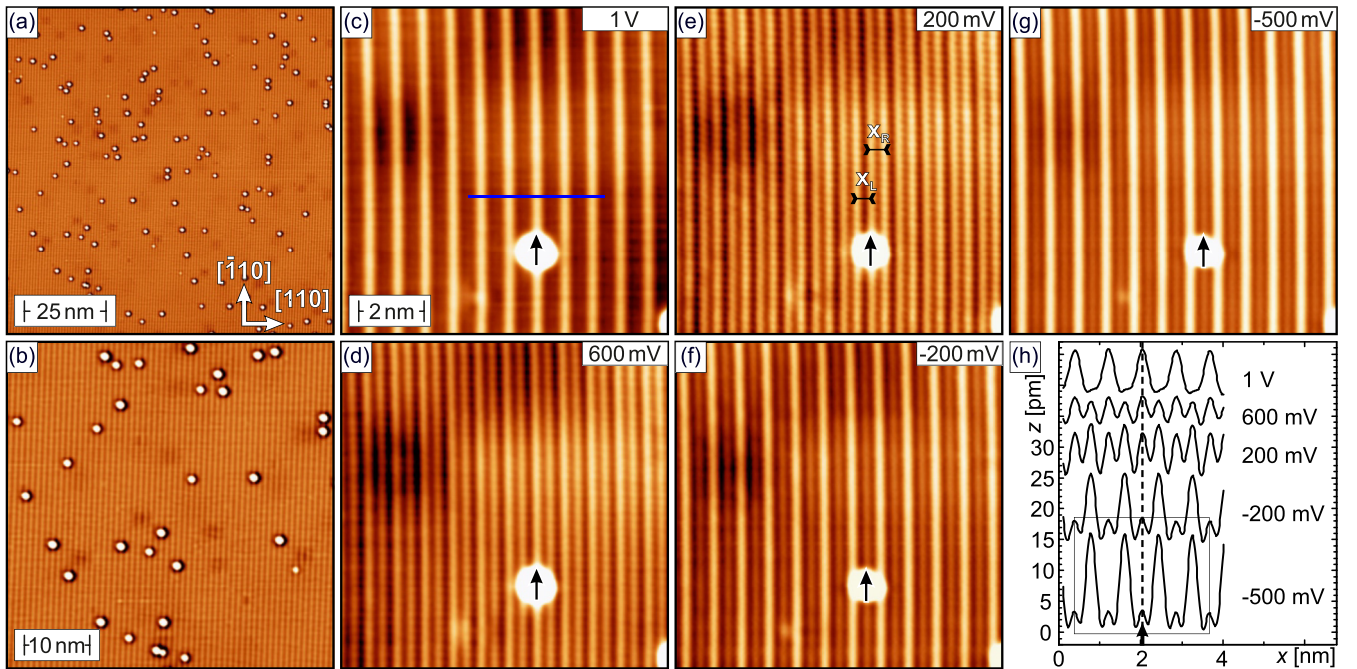


FIG. 8. (a) Overview and (b) higher-resolution scan on  $\text{CrO}_2$  chains on  $\text{Ir}(001)$ . (c)–(g) Bias-dependent STM images showing the same sample area. A cluster (marked by an arrow) serves as a position marker. A corrugation reversal is observed between panels (e) and (f), i.e., between  $U = 200$  mV and  $U = -200$  mV. (h) Line profiles measured along lines corresponding to the blue line in (c). Scan parameters: (a), (b)  $U = 1$  V,  $I = 300$  pA; (c)  $I = 2$  nA; (d), (g)  $I = 1.5$  nA; (e), (f)  $I = 0.5$  nA.

comparable to the interchain distance observed on the other quasi-one-dimensional TMO systems and consistent with the  $(3 \times 1)$  structural unit cell.

To study the electronic properties of this stripe pattern we performed the bias-dependent measurements presented in Figs. 8(c)–8(f). All scans show the same sample area as can be recognized by the cluster of unknown origin. An arrow marks the central region of this cluster and serves as a reference point during the following comparison. At a bias voltage  $U = 1$  V, Fig. 8(c), the arrow is aligned with the top of a stripe (A stripe). The next stripe to the right can be found about 1 nm apart just right of the bright cluster. When the bias voltage is reduced to  $U = 600$  mV, Fig. 8(d), another stripe (B stripe) appears between the A stripes. Interestingly, the corrugation is not mirror symmetric with respect to the plane defined by the  $[\bar{1}10]$  direction, i.e., along the stripes, and the (001) surface normal. This can best be recognized in the line sections shown in Fig. 8(h). The data have been extracted from the images shown in Figs. 8(c)–8(f) along traces corresponding to the blue line in panel (c). Again the arrow (and the hatched line) indicates the central position of the bright cluster. At  $U = 600$  mV the two minima left and right of the hatched line clearly exhibit different depth, with the left minimum being about 1 pm deeper than the right minimum. This trend becomes even stronger as the bias voltage is changed to  $U = 200$  meV. Furthermore, when decreasing the bias voltage further to  $U = -200$  meV, Fig. 8(f), and  $U = -500$  meV, Fig. 8(g), we observe that the corrugation of the B stripes becomes much larger than that of the A stripes. For example, at  $U = -500$  meV the corrugation of B stripes reaches  $(15 \pm 1)$  pm, whereas the corrugation of the A stripes only amounts to  $(2.6 \pm 0.3)$  pm.

Our bias-dependent experimental results on  $\text{CrO}_2/\text{Ir}(001)$  are strikingly different as compared to similar results on the other TMO chains. We find an asymmetric corrugation and A and B stripes which are the dominant features in topographic STM measurements performed at  $U > 200$  meV and  $U \leq -200$  meV, respectively. Furthermore, the change in corrugation is more pronounced for B stripes. Combined with the fact that the B stripes almost vanish for  $U = 1$  V we suppose that A stripes correspond to the  $\text{CrO}_2$  chains whereas the B stripes are assigned to the intermediate Ir double row. As detailed in Ref. [30] we performed SP-STM experiments on  $\text{CrO}_2/\text{Ir}(001)$  with both out-of-plane sensitive Cr/W and in-plane sensitive Fe/W tips. These measurements confirmed the structural  $(3 \times 1)$  unit cell of the  $\text{CrO}_2$  chains but did not provide any hint of a magnetically ordered state.

## B. TMO chains on $\text{Pt}(001)$

### 1. $\text{CoO}_2/\text{Pt}(001)$

Our SP-STM experiments of TMO chains on  $\text{Ir}(001)$  presented so far revealed a wide variety of spin structures. Whereas we could not detect any magnetic signal on  $\text{CoO}_2$  chains, suggesting a nonmagnetic state, for other  $3d$  elements we found collinear (anti)ferromagnetic (Fe) and a helical spin spiral order (Mn). It appears to be an obvious idea to extend the search for similar indirect DM-enhanced RKKY interactions by growing TMO chains on other heavy noble metals which also crystallize in the fcc structure. One candidate material is Pt, the direct neighbor of Ir in the periodic table of elements. In fact, it has already been shown that  $\text{CoO}_2$  chains can be grown by similar procedures on  $\text{Pt}(001)$  [11]. Since the  $\text{Pt}(001)$  reconstruction is stable against oxidation

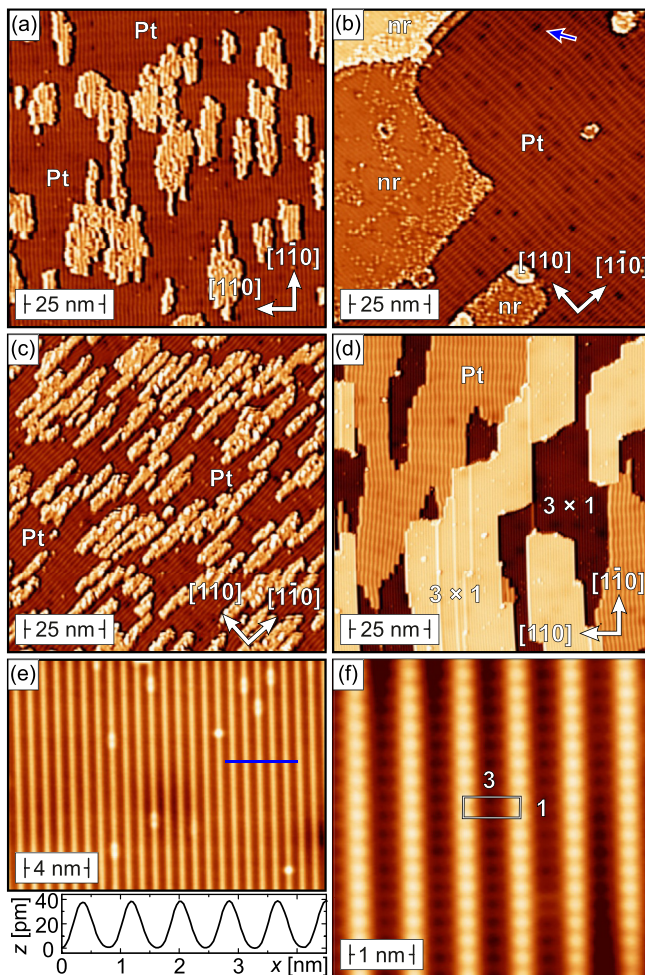


FIG. 9. Growth of  $\text{CoO}_2$  chains on  $\text{Pt}(001)$ . (a) Topography of  $\text{Co}/\text{Pt}(001)$  after evaporation on the warm substrate. (b) After oxidation of sample (a) no  $(3 \times 1)$  structure is observed. (c) Topography of  $\text{Co}/\text{Pt}(001)$  after evaporation on the cold substrate. (d) After oxidation of sample (c) a coexistence of  $\text{Pt}$  reconstruction and domains of  $\text{CoO}_2$  chains is observed. (e) Higher-resolution scan of the chains with line profile across the stripes. (f) Atomic-resolution scan with a nonmagnetic W tip confirms the structural  $(3 \times 1)$  unit cell. Scan parameters: (a)–(d)  $U = 1$  V,  $I = 300$  pA; (e)  $U = -100$  mV,  $I = 1.5$  nA; (f)  $U = 50$  mV,  $I = 5$  nA. All data measured with a nonmagnetic W tip.

we first studied the growth of Co on the clean surface [11]. In our STM images the complex hexagonal reconstructions of clean  $\text{Pt}(001)$  shows up as stripes with a periodicity of  $(1.36 \pm 0.15)$  nm [20]. Figure 9(a) shows the topography of a sample prepared by Co evaporation onto the warm surface resulting in the formation of  $(163 \pm 15)$  pm high islands which are elongated along the  $[1\bar{1}0]$  direction. This orientation correlates with the stripe direction of the  $\text{Pt}(001)$  surface and indicates preferential diffusion along the trenches of the reconstruction.

Annealing this sample in an oxygen atmosphere ( $p_{\text{O}_2} = 1 \times 10^{-7}$  mbar) at temperature  $T_{\text{ann}} \approx 920$  K results in the topography shown in Fig. 9(b). Two surface areas can be distinguished in these data which were measured with nonmagnetic W tips. In the upper right of Fig. 9(b) we again recognize the

clean  $\text{Pt}(001)$  surface which—similarly to our observations on clean  $\text{Ir}(001)$  [cf. blue arrow in Fig. 9(b)]—exhibits occasional circular depressions (density  $\approx 0.02$  nm $^{-2}$ ). The persistence of this reconstruction confirms the stability of the  $\text{Pt}(001)$  surface against oxidation. The remaining part of the surface is covered by islands without any oxygen-induced reconstruction (nr). Together with the unusual step height of  $(90 \pm 15)$  pm we interpret this as evidence for the formation of a  $\text{CoPt}$  surface alloy.

In a second attempt we initially cooled the clean  $\text{Pt}(001)$  surface in the LT-STM down to  $T \approx 5.5$  K. Subsequently the crystal was transferred to the preparation chamber for Co deposition onto the cold surface. Comparison of the resulting surface topography, Fig. 9(c), with the Co film grown at elevated temperature, Fig. 9(a), shows that low-temperature growth leads to smaller Co islands and the nucleation of very few second-layer Co islands. In contrast to the Co islands shown in Fig. 9(a) these low-temperature-deposited islands exhibit no stripes. Annealing this sample at the same parameters,  $T_{\text{ann}} \approx 920$  K, leads to the topography presented in Fig. 9(d), which is comparable to the earlier results of Ref. [11]. We can distinguish areas of reconstructed clean  $\text{Pt}(001)$  from extended and well-ordered regions showing the  $(3 \times 1)$  structure which is characteristic for  $\text{CoO}_2$  chains. The step height between domains of the same structure amounts to  $(199 \pm 10)$  pm, in perfect agreement with the value expected for  $\text{Pt}(001)$ . To complete the structural analysis we performed a higher-resolution scan which is presented in Fig. 9(e). Again pointlike defects are located on the stripes. The line profile taken at the position of the blue line confirms the periodicity of  $(830 \pm 20)$  pm. The inner structure of the stripes can be resolved by the atomic-resolution image shown in Fig. 9(f). Along the chains we measure a periodicity of  $(278 \pm 15)$  pm which agrees well with the cubic lattice vector expected for  $\text{Pt}$ ,  $a_{\text{Pt}} = 277$  pm [21].

After confirmation of the  $(3 \times 1)$  structure of  $\text{CoO}_2$  chains on  $\text{Pt}(001)$  [11] we attempted to resolve the spin or magnetic domain structure by means of SP-STM experiments using out-of-plane and in-plane polarized tips. However, these magnetically sensitive experiments [30] did not show a hint of the theoretically proposed AFM structure [11] nor could we detect any hint of other magnetically ordered states.

## 2. $\text{FeO}_2/\text{Pt}(001)$

For the preparation of  $\text{FeO}_2$  chains on  $\text{Pt}(001)$  we followed the same procedure as for Co, i.e., we started with the growth of Fe on the clean reconstructed  $\text{Pt}(001)$  surface. Indeed, Fe evaporation onto the warm  $\text{Pt}(001)$  substrate leads to a surface morphology very similar to  $\text{Co}/\text{Pt}(001)$  [cf. Figs. 9(a), 9(b); results for Fe not shown here] which we interpret as evidence for alloying with the substrate. To overcome this issue Fe was evaporated onto the cold sample and immediately oxidized at  $T \approx 870$  K. The resulting topography which is presented in the overview scan of Fig. 10(a) (scan size:  $300$  nm  $\times$   $300$  nm) shows plateaus and valleys with a typical lateral size of about  $50$  nm. They are separated by  $(199 \pm 15)$  pm high step edges preferentially oriented along high-symmetry directions of the substrate. Scanning a similar surface area at higher resolution, Fig. 10(b), reveals a stripe pattern with a periodicity of

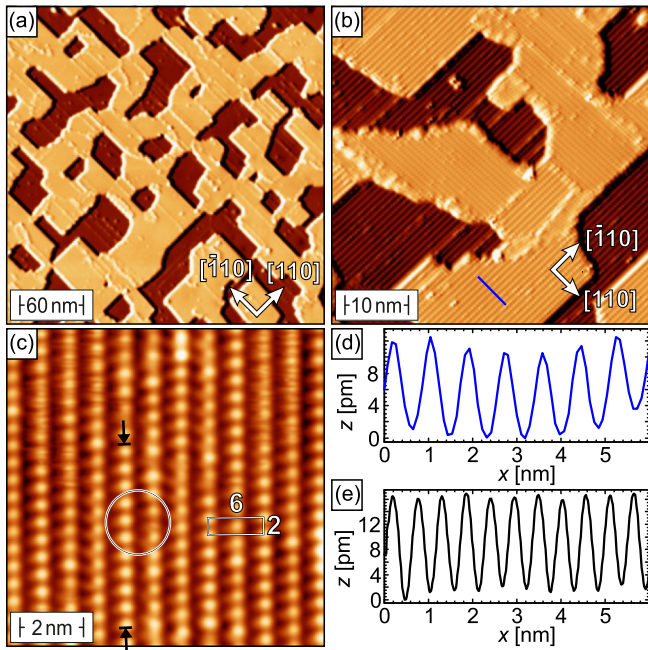


FIG. 10. (a) Overview scan of oxidized Fe on Pt(001). (b) A higher-resolution scan shows that terraces and islands exhibit a stripe pattern with the expected  $3a_{\text{Pt}}$  periodicity. (c) Atomic-scale image of oxidized Fe on Pt(001). Along the stripes the corrugation has a period of twice the atomic-lattice vector. Within the circle the order across the stripes changes from aligned to a shifted position. (d) Line profiles across (top) and along the stripes (bottom) at the positions of the blue line in (b) and at the position of the arrows in (c). Scan parameters: (a), (b)  $U = 1$  V,  $I = 300$  pA; (c)  $U = 100$  mV,  $I = 1$  nA. Nonmagnetic W tip.

( $844 \pm 40$ ) pm, as determined from the line profile in Fig. 10(d), in agreement with the  $(3 \times 1)$  reconstruction expected for  $\text{FeO}_2$  chains on Pt(001). Regions with stripes oriented in the  $[1\bar{1}0]$  or the  $[110]$  directions can be recognized. Surprisingly, atomic-scale images performed with nonmagnetic tips within a single domain are inconsistent with the expected structural  $(3 \times 1)$  unit cell. This can clearly be recognized by the image presented in Fig. 10(c) and the line section shown in Fig. 10(e) which was measured in between the two black arrows. The periodicity extracted from this line profile along the chains amounts to ( $543 \pm 25$ ) pm. This value is in good agreement with twice the lattice constant of Pt,  $2a_{\text{Pt}}$ . Furthermore, the maxima of adjacent stripes are out of phase in most cases. Therefore, our spin-averaged experimental data suggest the existence of a  $(6 \times 2)$  unit cell for the oxidized Fe on Pt(001) [see white box in Fig. 10(c)]. Since the positions of maxima and minima in a given chain are not completely static but slowly fluctuate, occasional exceptions from this rule can be observed. For example, the chain in the right part of the white circle in Fig. 10(c) shows such a switching event. Whereas the two chains marked by the circle are in phase in the lower part of the image, a phase shift by  $a_{\text{Pt}}$  in the right chain causes the two chains to be out of phase in the upper part of the image. Since the measurement of Fig. 10(c) was executed with a nonmagnetic tip and since the use of out-of-plane or in-plane sensitive magnetic probe tips did not

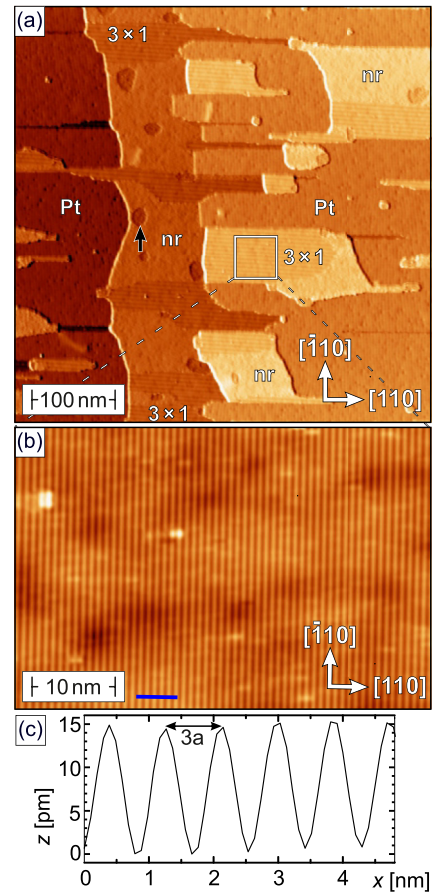


FIG. 11. (a) Overview scan of Pt(001) after Mn deposition and subsequent annealing in oxygen. In addition to reconstructed clean Pt(001) one also observes disordered (nr) and  $(3 \times 1)$ -reconstructed surface regions. (b) Higher-resolution scan at the position of the stripes. (c) Line profile measured along the blue line in (b) confirming the  $3a_{\text{Pt}}$  periodicity. Scan parameters:  $U = 1$  V,  $I = 300$  pA, nonmagnetic W tip.

result in any additional contrast, we have to conclude that the observed reconstruction has no magnetic origin but either a structural or an electronic origin. One possible explanation could be a Peierls instability due to a metal-insulator transition at low temperatures [36]. Further investigations are required to figure out the origin of the iron oxide phase.

### 3. $\text{MnO}_2/\text{Pt}(001)$

Finally we investigated  $\text{MnO}_2$  chains on Pt(001). In a first attempt we evaporated Mn while the Pt(001) substrate was held at room temperature and subsequently oxidized the sample at an oxygen pressure  $p_{\text{O}_2} = 1 \times 10^{-7}$  mbar at  $T \approx 920$  K. Unfortunately, this preparation procedure resulted in very small TMO domains with a size of (10...20) nm only. In order to improve surface homogeneity we reduced the oxygen pressure to  $p_{\text{O}_2} = 1 \times 10^{-8}$  mbar. The resulting topography measured with a nonmagnetic W tip is shown in Fig. 11(a). A significant fraction of the surface still exhibits the familiar reconstruction of the clean Pt(001) surface. In addition, two other kinds of surfaces could be

identified. The first one no longer shows any reconstruction (not reconstructed; nr) but is relatively rough. Similar findings have been reported for Cu/Ir(001) and were assigned to alloying [37]. Second, we found  $(3 \times 1)$ -reconstructed areas of  $\text{MnO}_2$ . For structural determination a higher-resolution scan measured on a homogeneously striped domain is shown in Fig. 11(b). Adjacent stripes are separated by  $(866 \pm 45)$  pm, as determined from the corresponding line profile in Fig. 11(c). We would like to emphasize that this particular structural domain exhibits a lateral size well above 50 nm, thereby allowing for the clear identification even of large magnetic unit cells. Moreover the surface exhibits very few defects. To exclude a behavior similar to what we have observed on oxidized Fe on Pt(001) we performed a detailed analysis of the observed contrasts. For example, line profiles measured along the chains marked with black arrows in Fig. 12(a) are presented in the upper part of Fig. 12(c). With a corrugation between 8.9 and 9.3 pm and an atomic spacing of  $(281 \pm 19)$  pm the data are in good agreement with a  $(3 \times 1)$  structure of  $\text{MnO}_2$  chains.

Such a sample surface was investigated by means of SP-STM using out-of-plane sensitive Cr-coated W tips. The resulting SP-STM image presented in Fig. 12(b) exhibits striking similarities if compared with the results obtained on  $\text{MnO}_2$  chains on Ir(001) [cf. Fig. 6(b)]. To analyze the spin-polarized measurement five line profiles which have been taken in between the colored arrows are plotted in the lower part of Fig. 12(c). Comparison with the spin-averaged data (black) reveals that—identically to our results obtained on  $\text{MnO}_2/\text{Ir}(001)$ —a doubling of the period along the chains can be recognized. This is a clear sign of an AFM intrachain coupling of the Mn atoms. In further analogy to the spin spiral system of  $\text{MnO}_2$  on Ir(001) the magnetic corrugation measured on the respective chains for  $\text{MnO}_2/\text{Pt}(001)$  is not constant but modulates periodically. For example, the line profiles clearly show that the green chain exhibits the lowest, almost vanishing corrugation. The other four chains constitute two groups which can be distinguished on the basis of the phase of their magnetic contrast. Whenever the two upper colored line profiles (orange, light blue) exhibit a maximum, the lower line profiles (red, dark blue) show a minimum. Since all line profiles possess a periodicity  $2a_{\text{Pt}}$  due to their AFM order along the chains, the phase difference shifts the magnetic contrast by  $a_{\text{Pt}}$ . This behavior can be explained by the model illustrated in Fig. 13(a). The coupling along the chains is assumed to be collinear AFM within each individual  $\text{MnO}_2$  chain. We initially assume a periodic modulation by a commensurate  $(15 \times 2)$  magnetic unit cell where the spin quantization axis of adjacent stripes rotates by  $72^\circ$ . Due to the dependence of the spin-polarized current on the angle between the tip magnetization and the spin quantization axis of the Mn atoms described by Eq. (1) this leads to a characteristic behavior of the magnetic corrugation. It is highest for the TMO chains which exhibit the highest projection onto the tip magnetization vector symbolized by a black arrow in Fig. 13(b), i.e., the light and dark blue chains. Their opposite perpendicular orientations will result in a  $\pi$  phase shift. A lower magnetic corrugation can be expected for the chains symbolized by orange and red arrows. The corrugation vanishes if the spin quantization axis of a chain is perpendicular

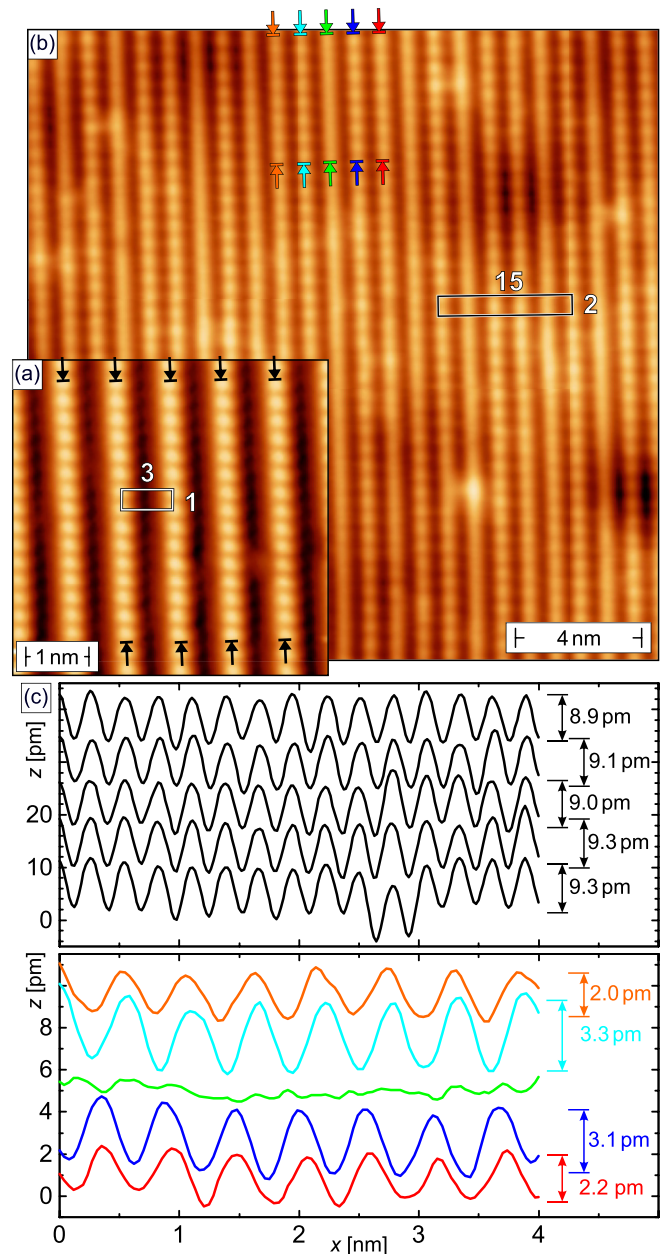


FIG. 12. (a) Atomic-resolution scan of  $\text{MnO}_2$  chains on Pt(001) performed with a W tip. (b) Spin-polarized measurement taken with a Cr-coated W tip. A periodic modulation of the chain-specific corrugation can clearly be seen. (c) Line profiles measured along five adjacent chains marked by correspondingly colored arrows as measured with a nonmagnetic (top) and a magnetic tip (bottom). Whereas a doubling of the period characteristic for an intrachain AFM coupling is observed on most of the chains, a pronounced modulation of the contrast is also visible across the chains. Scan parameters: (a)  $U = -5$  mV,  $I = 20$  nA; (b)  $U = 1$  V,  $I = 300$  pA.

to the tip polarization (green arrow). As a consequence of this rotating spin structure two chains will exhibit a parallel (light blue, orange) and two an antiparallel (blue, red) alignment with respect to the tip, thereby explaining the phase shift of  $a_{\text{Pt}}$  observed in Fig. 12(b). On the basis of this model we are able to determine the angle between the

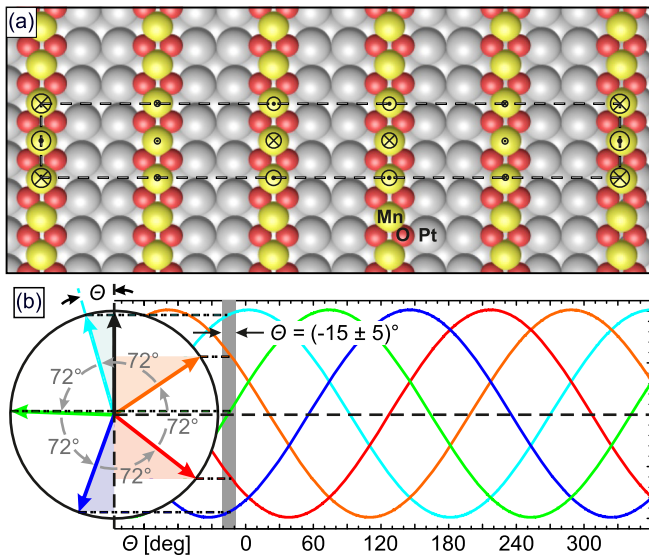


FIG. 13. (a) Schematic representation of a  $(15 \times 2)$  magnetic unit cell. A cycloidal spin spiral with out-of-plane rotating spins. The model in (b) is based on the magnetic corrugation in Fig. 12(c). From this a tilt  $\Theta = (-15 \pm 5)^\circ$  of the tip polarization with respect to the light blue chain with highest corrugation is seen.

magnetization direction of the tip and the light blue  $\text{MnO}_2$  chain to  $\Theta = (-15 \pm 5)^\circ$ .

SP-STM data measured with an in-plane sensitive Fe-coated W tip across a structural domain boundary indicate that the spin spiral possesses in-plane and out-of-plane contributions to the magnetization [30]. A similar spin spiral driven by the Dzyaloshinskii-Moriya interaction has already been found by DFT calculations for  $\text{MnO}_2$  chains on Ir(001) [14]. In agreement with the so-called Moriya rules [38] it is most natural to assume a cycloidal spin spiral with a Dzyaloshinskii-Moriya vector oriented along the chain direction. While the DMI is expected to be very similar for Ir and Pt due to their very similar atomic number, the higher occupation of the Pt  $5d$  shell causes significant differences in the respective Fermi surfaces. Indeed, it has been found that the RKKY-mediated oscillation period for (001)-oriented magnetic superlattices is about 50% longer for Co/Pt [39] than for Fe/Ir [40], in reasonable agreement with our observation of a periodicity which is also about 1.5 times as long. As we will show below deviations from the  $(15 \times 2)$  magnetic unit cell can be detected by imaging  $\text{MnO}_2$  chains on Pt(001) over larger surface areas. For example, Fig. 14 shows an SP-STM image with a scan area of  $30 \text{ nm} \times 30 \text{ nm}$ . For better visibility, the data set was filtered by using a bandpass. As described above SP-STM images of the  $(15 \times 2)$   $\text{MnO}_2/\text{Pt}(001)$  magnetic unit cell are characterized by fivefold periodicity of the structural  $(3 \times 1)$  unit cell. In general, the magnetization-direction-dependent variation of the total current gives rise to corrugation maxima if tip and sample are magnetized in the same direction, corrugation minima for an antiparallel alignment, or a very low or even vanishing corrugation if the angle between the tip and sample magnetization direction is close to  $90^\circ$  [cf. Eq. (1)]. At the  $y$  position marked by a dash-dotted white line at the bottom of Fig. 14 we find a sequence consisting of

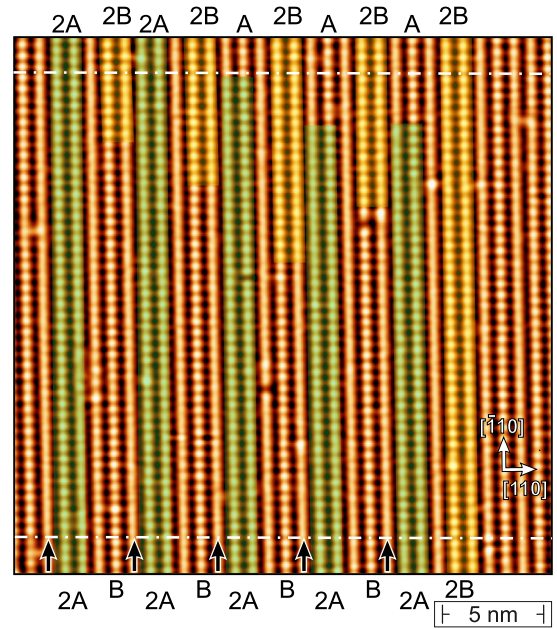


FIG. 14. Large SP-STM overview scan performed with a magnetic tip on  $\text{MnO}_2$  chains on Pt(001). The intrachain coupling is not strictly collinear, as can be recognized by inspecting the  $\text{MnO}_2$  chains marked by black arrows. Whereas no significant magnetic contrast is detected in the bottom part, a strong magnetic contrast with a  $2a_{\text{Pt}}$  periodicity is clearly visible in the upper part of the image.

two  $\text{MnO}_2$  chains which exhibit corrugation maxima (colored green, labeled 2A), then one chain with a low contrast, one  $\text{MnO}_2$  chain with corrugation minima (B), and finally a chain with no recognizable spin contrast (marked by black arrows). Close inspection of the data set presented in Fig. 14 reveals that the contrast of the specific  $\text{MnO}_2$  chains is not constant but slowly varies. For example, the  $\text{MnO}_2$  chains marked by black arrows which showed a vanishingly low magnetic contrast at the bottom of Fig. 14 develop a sizable magnetic contrast toward the top part of the scan. This observation indicates that the magnetic order along the  $\text{MnO}_2$  chains is not strictly collinear but slightly canted. Within our field of view of  $30 \text{ nm}$  along the  $[\bar{1}10]$  direction, however, we only observe about a quarter of a  $2\pi$  rotation. Therefore, we can conclude that the wavelength of the magnetic structure along the  $\text{MnO}_2$  chains on Pt(001) must be very long, probably of the order of  $100 \text{ nm}$ .

As a result of the spin rotation along the  $\text{MnO}_2$  chains and the existence of occasional structural defects the magnetic order is not strictly periodic. In fact, comparison of the bottom part of the SP-STM image with the top part of Fig. 14 reveals that the contrast changed. Whereas the sequence of contrasts obtained within the five TMO chains of a magnetic unit cell was 2A-low-B-low in the bottom part, the dominating sequence in the upper part is A-low-2B-low. At the moment we can only speculate about the origin of this noncollinearity along the chains. Possibly, DM-type interactions triggered by the overlap of the O  $2p$  with Ir  $5d$  orbitals also influence the superexchange along the TMO chains.

#### IV. CONCLUSION

In summary, we systematically investigated the structural and magnetic properties of transition metal oxides (TMOs) on the fcc(001) surfaces of Ir and Pt. We find that Co, Fe, and Mn form quasi-one-dimensional TMO chains with a  $(3 \times 1)$  unit cell. Similar  $(3 \times 1)$ -ordered chains were observed for Cr on Ir(001). Whereas no magnetic signal was found for Co- and Cr-based chains, our SP-STM measurements confirm the theoretically predicted antiferromagnetic intrachain coupling for  $\text{FeO}_2/\text{Ir}(001)$  and for  $\text{MnO}_2$  chains on both substrates. A ferromagnetic interchain coupling is found for  $\text{FeO}_2/\text{Ir}(001)$ . In the case of  $\text{MnO}_2$  the SP-STM images reveal a complex helical intrachain magnetic coupling, resulting in a  $(9 \times 2)$  magnetic unit cell on Ir(001) and a  $(15 \times 2)$  magnetic unit cell for Pt(001). Furthermore, large-scale SP-STM images of  $\text{MnO}_2$  chains on Pt(001) unveil that also the intrachain

magnetic coupling is not perfectly collinear but slightly canted, resulting in a spin spiral with a periodicity corresponding to several hundred substrate atoms. Our results highlight the relevance of spin-orbit-related effects for magnetic coupling phenomena in systems with broken inversion symmetry, such as surfaces or nanoparticles.

#### ACKNOWLEDGMENTS

Experimental work was supported by DFG through FOR 1700 (project E6), SPP 2137 “Skyrmionics” (BO 1468/26-1), and by the Dresden-Würzburg Center for Topological Quantum Matter Research (ct.qmat). The authors would like to thank Paolo Moras (Trieste, Italy) for bringing one-dimensional TMOs to our attention and Jens Kügel (Würzburg, Germany) for critically reading the manuscript.

- 
- [1] C. A. F. Vaz, J. A. C. Bland, and G. Lauhoff, Magnetism in ultrathin film structures, *Rep. Prog. Phys.* **71**, 056501 (2008).
- [2] H.-B. Braun, Topological effects in nanomagnetism: From superparamagnetism to chiral quantum solitons, *Adv. Phys.* **61**, 1 (2012).
- [3] M. Bode, Spin-polarized scanning tunneling microscopy, *Rep. Prog. Phys.* **66**, 523 (2003).
- [4] A. Kubetzka, P. Ferriani, M. Bode, S. Heinze, G. Bihlmayer, K. von Bergmann, O. Pietzsch, S. Blügel, and R. Wiesendanger, Revealing Antiferromagnetic Order of the Fe Monolayer on W(001): Spin-Polarized Scanning Tunneling Microscopy and First-Principles Calculations, *Phys. Rev. Lett.* **94**, 087204 (2005).
- [5] M. Bode, E. Y. Vedmedenko, K. von Bergmann, A. Kubetzka, P. Ferriani, S. Heinze, and R. Wiesendanger, Atomic spin structure of antiferromagnetic domain walls, *Nat. Mater.* **5**, 477 (2006).
- [6] C. L. Gao, W. Wulfhekel, and J. Kirschner, Revealing the  $120^\circ$  Antiferromagnetic Néel Structure in Real Space: One Monolayer Mn on Ag(111), *Phys. Rev. Lett.* **101**, 267205 (2008).
- [7] M. Bode, S. Heinze, A. Kubetzka, O. Pietzsch, M. Hennefarth, M. Getzlaff, R. Wiesendanger, X. Nie, G. Bihlmayer, and S. Blügel, Structural, electronic, and magnetic properties of a Mn monolayer on W(110), *Phys. Rev. B* **66**, 014425 (2002).
- [8] S. Heinze, M. Bode, A. Kubetzka, O. Pietzsch, X. Nie, S. Blügel, and R. Wiesendanger, Real-space imaging of two-dimensional antiferromagnetism on the atomic scale, *Science* **288**, 1805 (2000).
- [9] M. Bode, M. Heide, K. von Bergmann, P. Ferriani, S. Heinze, G. Bihlmayer, A. Kubetzka, O. Pietzsch, S. Blügel, and R. Wiesendanger, Chiral magnetic order at surfaces driven by inversion asymmetry, *Nature (London)* **447**, 190 (2007).
- [10] P. Ferstl, L. Hammer, C. Sobel, M. Gubo, K. Heinz, M. A. Schneider, F. Mittendorfer, and J. Redinger, Self-Organized Growth, Structure, and Magnetism of Monatomic Transition-Metal Oxide Chains, *Phys. Rev. Lett.* **117**, 046101 (2016).
- [11] P. Ferstl, F. Mittendorfer, J. Redinger, M. A. Schneider, and L. Hammer, Monatomic Co,  $\text{CoO}_2$ , and  $\text{CoO}_3$  nanowires on Ir(100) and Pt(100) surfaces: Formation, structure, and energetics, *Phys. Rev. B* **96**, 085407 (2017).
- [12] A. Krönlein, M. Schmitt, M. Hoffmann, J. Kemmer, N. Seubert, M. Vogt, J. Küspert, M. Böhme, B. Alonazi, J. Kügel, H. A. Albrithen, M. Bode, G. Bihlmayer, and S. Blügel, Magnetic Ground State Stabilized by Three-Site Interactions: Fe/Rh(111), *Phys. Rev. Lett.* **120**, 207202 (2018).
- [13] N. Romming, H. Pralow, A. Kubetzka, M. Hoffmann, S. von Malottki, S. Meyer, B. Dupé, R. Wiesendanger, K. von Bergmann, and S. Heinze, Competition of Dzyaloshinskii-Moriya and Higher-Order Exchange Interactions in Rh/Fe Atomic Bilayers on Ir(111), *Phys. Rev. Lett.* **120**, 207201 (2018).
- [14] M. Schmitt, P. Moras, G. Bihlmayer, R. Cotsakis, M. Vogt, J. Kemmer, A. Belabbes, P. M. Sheverdyaeva, A. K. Kundu, C. Carbone, S. Blügel, and M. Bode, Indirect chiral magnetic exchange through Dzyaloshinskii-Moriya-enhanced RKKY interactions in manganese oxide chains on Ir(100), *Nat. Commun.* **10**, 2610 (2019).
- [15] A. A. Khajetoorians, M. Steinbrecher, M. Ternes, M. Bouhassoune, M. dos Santos Dias, S. Lounis, J. Wiebe, and R. Wiesendanger, Tailoring the chiral magnetic interaction between two individual atoms, *Nat. Commun.* **7**, 10620 (2016).
- [16] J. Hermenau, J. Ibañez-Azpiroz, C. Hübner, A. Sonntag, B. Baxevanis, K. T. Ton, M. Steinbrecher, A. A. Khajetoorians, M. dos Santos Dias, S. Blügel, R. Wiesendanger, S. Lounis, and J. Wiebe, A gateway towards non-collinear spin processing using three-atom magnets with strong substrate coupling, *Nat. Commun.* **8**, 642 (2017).
- [17] J. T. Grant, A LEED study of the Ir(100) surface, *Surf. Sci.* **18**, 228 (1969).
- [18] T. N. Rhodin and G. Brodén, Preparation and chemisorptive properties of the clean normal and reconstructed surfaces of Ir(100): Role of multiplets, *Surf. Sci.* **60**, 466 (1976).
- [19] A. Schmidt, W. Meier, L. Hammer, and K. Heinz, Deep-going reconstruction of Ir(100)- $5 \times 1$ , *J. Phys.: Condens. Matter* **14**, 12353 (2002).

- [20] R. Hammer, K. Meinel, O. Krahn, and W. Widdra, Surface reconstruction of Pt(001) quantitatively revisited, *Phys. Rev. B* **94**, 195406 (2016).
- [21] A. E. Morgan and G. A. Somorjai, Low energy electron diffraction studies of gas adsorption on the platinum (100) single crystal surface, *Surf. Sci.* **12**, 405 (1968).
- [22] O. Pietzsch, A. Kubetzka, M. Bode, and R. Wiesendanger, Real-Space Observation of Dipolar Antiferromagnetism in Magnetic Nanowires by Spin-Polarized Scanning Tunneling Spectroscopy, *Phys. Rev. Lett.* **84**, 5212 (2000).
- [23] M. Bode, O. Pietzsch, A. Kubetzka, S. Heinze, and R. Wiesendanger, Experimental Evidence for Intra-Atomic Non-collinear Magnetism at Thin Film Probe Tips, *Phys. Rev. Lett.* **86**, 2142 (2001).
- [24] S. Meckler, N. Mikuszeit, A. Preßler, E. Y. Vedmedenko, O. Pietzsch, and R. Wiesendanger, Real-Space Observation of a Right-Rotating Inhomogeneous Cycloidal Spin Spiral by Spin-Polarized Scanning Tunneling Microscopy in a Triple Axes Vector Magnet, *Phys. Rev. Lett.* **103**, 157201 (2009).
- [25] M. Bode, M. Getzlaff, and R. Wiesendanger, Spin-Polarized Vacuum Tunneling into the Exchange-Split Surface State of Gd(0001), *Phys. Rev. Lett.* **81**, 4256 (1998).
- [26] L. Berbil-Bautista, S. Krause, M. Bode, and R. Wiesendanger, Spin-polarized scanning tunneling microscopy and spectroscopy of ferromagnetic Dy(0001)/W(110) films, *Phys. Rev. B* **76**, 064411 (2007).
- [27] R. Ravlić, M. Bode, A. Kubetzka, and R. Wiesendanger, Correlation of dislocation and domain structure of Cr(001) investigated by spin-polarized scanning tunneling microscopy, *Phys. Rev. B* **67**, 174411 (2003).
- [28] Ph. Kurz, G. Bihlmayer, and S. Blügel, Magnetism and electronic structure of hcp Gd and the Gd(0001) surface, *J. Phys.: Condens. Matter* **14**, 6353 (2002).
- [29] J. W. Arblaster, Crystallographic properties of iridium, *Platinum Met. Rev.* **54**, 93 (2010).
- [30] See Supplemental Material at <http://link.aps.org/supplemental/10.1103/PhysRevB.100.054431> for detailed information regarding the preparation of clean, oxygen-reconstructed, and TMO-covered fcc(001) surfaces, the characterization of magnetic probe tips, and SP-STM investigations of TMOs not discussed in the main text, including Refs. [41–49].
- [31] P. W. Anderson, Antiferromagnetism. Theory of superexchange interaction, *Phys. Rev.* **79**, 350 (1950).
- [32] A. Fert and Peter M. Levy, Role of Anisotropic Exchange Interactions in Determining the Properties of Spin-Glasses, *Phys. Rev. Lett.* **44**, 1538 (1980).
- [33] B. Dupé, J. E. Bickel, Y. Mokrousov, F. Otte, K. von Bergmann, A. Kubetzka, S. Heinze, and R. Wiesendanger, Giant magnetization canting due to symmetry breaking in zigzag Co chains on Ir(001), *New J. Phys.* **17**, 023014 (2015).
- [34] J. Bouaziz, M. dos Santos Dias, A. Ziane, M. Benakki, S. Blügel, and S. Lounis, Chiral magnetism of magnetic adatoms generated by Rashba electrons, *New J. Phys.* **19**, 023010 (2017).
- [35] S. V. Grigoriev, Yu. O. Chetverikov, D. Lott, and A. Schreyer, Field Induced Chirality in the Helix Structure of Dy/Y Multilayer Films and Experimental Evidence for Dzyaloshinskii-Moriya Interaction on the Interfaces, *Phys. Rev. Lett.* **100**, 197203 (2008).
- [36] A. van Houselt, T. Gnielka, J. M. J. Aan de Brugh, N. Oncel, D. Kockmann, R. Heid, K.-P. Bohnen, B. Poelsema, and H. J. W. Zandvliet, Peierls instability in Pt chains on Ge(001), *Surf. Sci.* **602**, 1731 (2008).
- [37] Gerhard Gilarowski, Javier Méndez, and Horst Niehus, Initial growth of Cu on Ir(100)-(5 × 1), *Surf. Sci.* **448**, 290 (2000).
- [38] T. Moriya, Anisotropic superexchange interaction and weak ferromagnetism, *Phys. Rev.* **120**, 91 (1960).
- [39] J. Moritz, F. Garcia, J. C. Toussaint, B. Dieny, and J. P. Nozières, Orange peel coupling in multilayers with perpendicular magnetic anisotropy: Application to (Co/Pt)-based exchange-biased spin-valves, *Europhys. Lett.* **65**, 123 (2004).
- [40] D. Stoeffler, *Ab initio* study of the Fe intra- and inter-layer magnetic order in Fe/Ir(001) superlattices, *Eur. Phys. J. B* **37**, 311 (2004).
- [41] K. Johnson, Q. Ge, S. Titmuss, and D. A. King, Unusual bridged site for adsorbed oxygen adatoms: Theory and experiment for Ir{100}-(1 × 2)-O, *J. Chem. Phys.* **112**, 10460 (2000).
- [42] P. Ferstl, T. Schmitt, M. A. Schneider, L. Hammer, A. Michl, and S. Müller, Structure and ordering of oxygen on unreconstructed Ir(100), *Phys. Rev. B* **93**, 235406 (2016).
- [43] H. J. Elmers, J. Hauschild, and U. Gradmann, Onset of perpendicular magnetization in nanostripe arrays of Fe on stepped W(110) surfaces, *Phys. Rev. B* **59**, 3688 (1999).
- [44] M. Bode, S. Heinze, A. Kubetzka, O. Pietzsch, X. Nie, G. Bihlmayer, S. Blügel, and R. Wiesendanger, Magnetization-Direction-Dependent Local Electronic Structure Probed by Scanning Tunneling Spectroscopy, *Phys. Rev. Lett.* **89**, 237205 (2002).
- [45] O. Pietzsch, A. Kubetzka, M. Bode, and R. Wiesendanger, Observation of magnetic hysteresis at the nanometer scale by spin-polarized scanning tunneling spectroscopy, *Science* **292**, 2053 (2001).
- [46] A. Kubetzka, O. Pietzsch, M. Bode, and R. Wiesendanger, Spin-polarized scanning tunneling microscopy study of 360° walls in an external magnetic field, *Phys. Rev. B* **67**, 020401(R) (2003).
- [47] M. Bode, A. Kubetzka, S. Heinze, O. Pietzsch, R. Wiesendanger, M. Heide, X. Nie, G. Bihlmayer, and S. Blügel, Spin-orbit induced local band structure variations revealed by scanning tunneling spectroscopy, *J. Phys.: Condens. Matter* **15**, S679 (2003).
- [48] E. Y. Vedmedenko, A. Kubetzka, K. von Bergmann, O. Pietzsch, M. Bode, J. Kirschner, H. P. Oepen, and R. Wiesendanger, Domain Wall Orientation in Magnetic Nanowires, *Phys. Rev. Lett.* **92**, 077207 (2004).
- [49] H. J. Elmers, J. Hauschild, H. Fritzsche, G. Liu, U. Gradmann, and U. Köhler, Magnetic Frustration in Ultrathin Fe Films, *Phys. Rev. Lett.* **75**, 2031 (1995).